Geophysical Journal International

*Geophys. J. Int.* (2013) **195,** 1184–1195
Advance Access publication 2013 August 13

doi: 10.1093/gji/ggt285

# Observations of changing anisotropy across the southern margin of the African LLSVP

Sanne Cottaar[1] and Barbara Romanowicz[1,2,3]

[1]*Berkeley Seismological Laboratory, UC Berkeley,* 215 *McCone Hall* 4760*, Berkeley, CA* 94720*, USA. E-mail: sanne@berkeley.edu*
[2]*Collège de France,* 11*, Place Marcelin Berthelot,* 75231 *Paris Cedex* 05*, France*
[3]*Institut de Physique du Globe,* 1*, rue Jussieu,* 75238 *Paris Cedex* 05*, France*

Accepted 2013 July 15. Received 2013 July 3; in original form 2013 April 15

## SUMMARY

We present evidence for the presence of complex anisotropy in the lowermost mantle from 3-D waveform modelling of observed core-diffracted shear waves that sample the southern edge of the African Large Low Shear Velocity Province (LLSVP). The anomalously strong amplitude of the *SV* component for the shear core-diffracted phase at large distances indicates the presence of anisotropy. We measure shear wave splitting parameters to determine which part of the elastic tensor is constrained by this particular data set. The modelling is performed using the spectral element method. The anisotropy is strong outside the LLSVP, weakens or rotates close to its boundary, and appears to be absent inside the LLSVP. The presence of the LLSVP margin may cause flow in the mantle to change direction. The occurrence of strong anisotropy in the region of fast seismic velocities is compatible with lattice-preferred orientation in post-perovskite due to accommodation of flow through dislocation creep.

**Key words:** Mantle processes; Body waves; Seismic anisotropy.



## 1 INTRODUCTION

Much of our knowledge on the distribution and characteristics of heterogeneity in the interior of our planet comes from the study of seismic wave velocities. Specifically, the study of seismic anisotropy (i.e. the variation of seismic wave speeds with direction of propagation and polarization) provides information about the direction of material flow and therefore constrains the dynamics in the interior (e.g. Karato 1998a). In the Earth, seismic anisotropy appears strong in the upper mantle and the lowermost lower mantle (D″); that is, in boundary layers where strains caused by horizontal flow tend to be large (e.g. Montagner 1998). Some seismic anisotropy may also be present in the mantle transition zone (Trampert & van Heijst 2002) and in the inner core (Woodhouse *et al.* 1986; Morelli *et al.* 1986).

Anisotropy in the upper mantle has been linked to flow in the asthenosphere and the subsequent deformation and preferred orientation of intrinsically seismically anisotropic olivine (e.g. Karato 1998b). An olivine single crystal is seismically fast along its *a*-axis (Mainprice *et al.* 2000). Dislocation creep on preferred slip planes along preferred slip directions (together forming a slip system) in the olivine crystals accommodates the flow. The subsequent preferred alignment along these slip systems produces seismic anisotropy at the polycrystal scale. The resulting signature of anisotropy, however, ultimately depends on which slip system is preferred, which for olivine depends on stress and water content (Mainprice 2007; Karato *et al.* 2008). This makes interpretation of observed seismic anisotropy under different tectonic environments somewhat ambiguous.

Even less is known about interpreting seismic anisotropy in terms of flow in D″, although there have been recent advances (see overview in Nowacki *et al.* 2011). First, it is unclear if the lowermost mantle is composed of perovskite (Pv) or post-perovskite (pPv), or if the composition varies laterally (e.g. Mosca *et al.* 2012). These two mineral phases have intrinsically different single crystal anisotropy (Stackhouse *et al.* 2005; Wentzcovitch *et al.* 2006). Secondly, interpretation will depend on the dominant lattice plane along which deformation by dislocation creep occurs. The same slip system is consistently measured for Pv (e.g. Wenk *et al.* 2011), but remains ambiguous for pPv (e.g. Miyagi *et al.* 2011). Different dominant slip systems for pPv result in opposite signatures in radial anisotropy (Walker *et al.* 2011; Wenk *et al.* 2011). Finally, it is uncertain if dislocation creep occurs in the lowermost mantle, or if deformation is dominated by diffusion creep (McNamara *et al.* 2001). The latter would not result in seismic anisotropy.

Ultimately, observations of seismic anisotropy need to be linked to numerical geodynamical models to confirm the conditions under which mapped flow occurs. There are a number of factors that can largely influence the models proposed for the lowermost mantle. One is the role of possibly chemically distinct Large Low Shear Velocity Provinces (LLSVPs; Garnero & McNamara 2008; Lekic *et al.* 2012), which can largely change the pattern of flow (McNamara & Zhong 2005; Steinberger & Torsvik 2012). Also little is known

about the strength, and the subsequent bending, squishing or buckling, of the slabs as they reach the core–mantle boundary (CMB; Loubet *et al.* 2009). Constraining seismic anisotropy can provide clarifications on the assumptions made in these models.

Besides mineralogical and geodynamical uncertainties, seismological observations have certain limitations, as the full 3-D anisotropic signature is never resolved. One can only constrain those components of the present elastic anisotropy that the seismic data set is sensitive to, and the resolution is limited to the wavelengths of the observed waves. The signature and resolution of a heterogeneous medium that can be mapped by seismic waves is called the effective medium. Intrinsically isotropic material can result in anisotropy in the effective medium, for example when layering or other heterogeneity is present (Crampin 1984). This non-uniqueness adds a degree of complexity to the interpretation of observations of anisotropy. Different seismic phases will be more sensitive to the presence of different modes of anisotropy. The main considered modes are radial and azimuthal anisotropy. In general, hexagonal symmetry is assumed when interpreting seismological data, and in that case five elastic constants and two angles describing the tilt of the axis of symmetry are needed to describe the anisotropy. Radial anisotropy, where the symmetry axis is vertical, is commonly observed in D″, from forward waveform modelling (e.g. Vinnik *et al.* 1995; Garnero & Lay 1997) or by tomographic in version (Panning & Romanowicz 2006; Kustowski *et al.* 2008; Kawai & Geller 2010). In the case of azimuthal anisotropy, on the other hand, seismic velocity varies as a function of azimuth in the horizontal plane, which remains difficult to constrain in D″ due to limited azimuthal coverage. Local studies constrain the azimuthal component of the elastic tensor from *SKS*-*SKKS* differential splitting measurements (Niu & Perez 2004; Restivo & Helffrich 2006; Wang & Wen 2007; Long 2009; Lynner & Long 2012) and with *ScS* waves (Garnero *et al.* 2004; Maupin 2005; Thomas *et al.* 2007; Nowacki *et al.* 2010). The latter gives improved azimuthal constraints when crossing rays are available (Wookey & Kendall 2008), otherwise only the tilted anisotropy component orthogonal to the direction of propagation can be constrained. Here, we apply shear wave splitting analysis to shear diffracted waveforms at large distances.

In Section 2.1, we describe the methodological approach using shear wave splitting and forward modelling. In Section 3, we introduce the anomalous observations of $S_{\rm diff}$ from a Fiji event towards the Kaapvaal array in Africa. From the analysis of the data, we argue that the strong arrival of $S_{\rm diff}$ on the radial component is not dominated by the presence of anisotropy in the upper mantle, but rather is caused by the presence of tilted anisotropy in D″. Through shear wave splitting, we constrain the average fast axis direction. Additional confirmation comes from the computation of synthetic waveforms (Section 4) for anisotropic models using a numerical spectral element method. The forward modelling also allows us to constrain the lateral and radial extent of the anisotropy.

## 2 METHODS

### 2.1 Shear wave splitting measurements in $S_{\rm diff}$

Shear diffracted waves ($S_{\rm diff}$) at large distances become polarized along the *SH* component. The *SV* component attenuates along the diffracted path due to *P*-*SV* coupling with the outer core (Teng & Richards 1976; Doornbos & Mondt 1980; Maupin 1994; Komatitsch *et al.* 2010). This effect, which gets stronger as a function of distance, is illustrated by synthetics in Fig. 1 for three

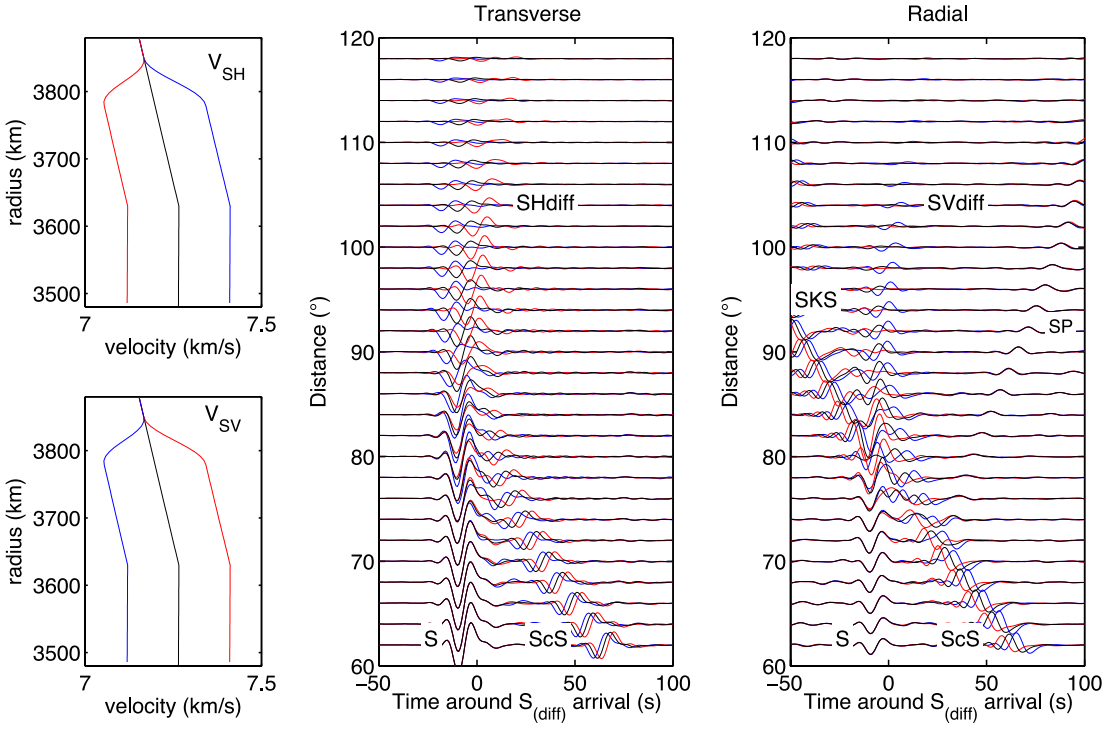


**Figure 1.** Velocity models (left-hand side) and synthetic waveforms (right-hand side) for transverse isotropic models. Black models and seismograms are for PREM. The blue (respectively, red) velocity model has $V_{SH}$ 2 per cent faster (resp. slower) and $V_{SV}$ 2 per cent slower (resp. faster) than PREM in the lowermost 300 km of the mantle. Both models are smoothed towards PREM over 70 km. This synthetic test illustrates the fast decay of $SV_{\rm diff}$, even when $V_{SV}$ is slow, in the shadow of the core. In addition, the integrated traveltime difference between $SH$ − and $SV_{\rm diff}$ increases strongly at these distances. Transverse isotropy causes no coupling between the *SV* and *SH* component as the lack of an *SKS* arrival on the *SH* components illustrates.

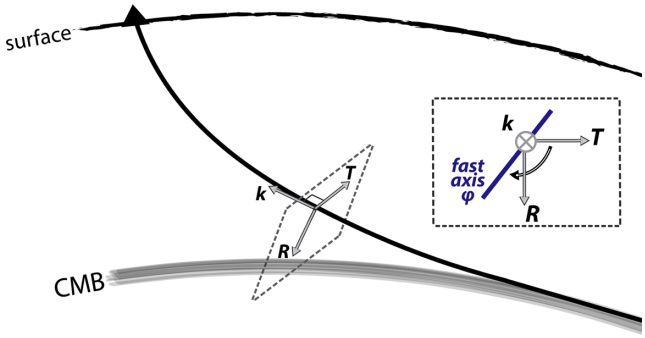


**Figure 2.** Definition of ($R$, $T$, $k$) reference frame and the fast axis $\phi_f$ within it.

different velocity models. The *SV* component is negligibly small beyond 110°. The polarization along one component gives the analysis of the $S_{diff}$ phase at large distances the same advantage as the analysis of *SKS* when measuring shear wave splitting in upper-mantle studies; while the *SKS* phase has a known initial polarization on the radial component, the $S_{diff}$ phase is polarized on the transverse component at large distances. In addition, in the case of $S_{diff}$, any interaction between the *SH* and *SV* components due to source-side upper mantle or D″ anisotropy can be ignored. Indeed, any resulting energy on the *SV* component from coupling on the source side will attenuate out along the diffracted part of the path. The only effect of anisotropy on $S_{diff}$ on the source side is a decrease in the amplitude of the final *SH* component through coupling with *SV* and loss of energy to the outer core.

In *SKS* studies, the incident angle of the *SKS* phase is (near-)vertical, subsequently the measured splitting reveals the presence of anisotropy in the horizontal plane, orthogonal to the direction of propagation. For an $S_{diff}$ phase turning upwards in the D″, the incidence angle will vary as a function of position along the path. The shear wave splitting in the phase will only be sensitive to anisotropy in the plane ($R$, $T$) orthogonal to its direction of propagation ($k$). In Fig. 2, we define the fast axis $\phi_f$ in the reference frame of the phase.

Given that the initial polarization is known, one can apply any of the single-station methods that are applied to measure splitting in the case of *SKS*. Here, we have applied the 'rotation-correlation' or 'cross-correlation' method (Bowman & Ando 1987) as implemented in SplitLab (Wüstefeld *et al.* 2008). This method rotates the horizontal components and calculates the cross-correlation values between the two rotated components for all possible angles. The maximum cross-correlation coefficient corresponds to the rotation angle at which the fast and slow waveforms are most orthogonal. This rotation angle is the fast axis direction $\phi_f$. The splitting time d$t$ is the shift between the fast and slow waveforms after rotation. We compare the results of this method with methods that grid search to attempt to minimize the energy on the radial component and eigenvalue methods (Vinnik *et al.* 1989; Silver & Chan 1991). For stations with strong splitting, the two methods give similar results; while only the rotation-correlation method results in small splitting times for the null measurements. Using both methods, we evaluate the measurements through the quality index defined in Wuestefeld *et al.* (2010) which helps to identify null measurements. We additionally apply these methods to the *SKS* and *SKKS* phases from the same event to measure the amount of splitting resulting from the upper mantle.

### 2.2 Full waveform modelling with coupled spectral element method (CSEM)

Forward modelling of full waveforms in various anisotropic models is performed using the 'sandwiched' version of the CSEM (Capdeville *et al.* 2002, 2003). CSEM solves the wave equation using the spectral element method in the mantle, while it solves a normal-mode solution for a 1-D velocity model in the core. The two are connected at the CMB through a Dirichlet-to-Neumann operator. The sandwiched version of CSEM applies the 1-D normal-mode solution both in the core and in most of the mantle, and only solves the fully 3-D case in one layer: in our case the lowermost 370 km of the mantle. For our application of repeated simulations for the same event for different 3-D models in D″, this method is computationally advantageous, as the normal-mode computation is fast and only needs to be done once per event. We have extended the sandwiched CSEM code to include fully anisotropic tensors in the velocity model.

We describe the anisotropy in our models in terms of variation of the two shear velocities as a function of azimuth $\phi$ on a plane (following Montagner *et al.* 2000):

$$\rho V_{S1}^2 = \rho V_S^2 + G_C \cos 2\phi + G_S \sin 2\phi, \tag{1}$$

$$\rho V_{S2}^2 = \rho V_S^2 - G_C \cos 2\phi - G_S \sin 2\phi, \tag{2}$$

where the $G_C$ and $G_S$ terms can be defined in terms of the fast direction $\phi_f$, and the strength of anisotropy $G = \sqrt{G_C^2 + G_S^2} = (fraction\ of\ anisotropy) * \rho V_S^2$:

$$G_C = sign(\cos 2\phi_f)\sqrt{\frac{G}{\tan^2 2\phi_f + 1}}, \tag{3}$$

$$G_S = sign(\sin 2\phi_f)\sqrt{G^2 - G_C^2}. \tag{4}$$

Initially, we define the isotropic stiffness tensor (described by the Lamé parameters $\lambda$ and $\mu$) in the (*fast*, *slow*, $k$)-reference frame in the Voigt notation. We introduce shear wave anisotropy in the (*fast*, *slow*)-plane by perturbing C44 negatively by $G_C$, C55 positively by $G_C$ and setting C45 to $G_S$:

$$C_{IJ} = \begin{pmatrix} \lambda+2\mu & \lambda & \lambda & 0 & 0 & 0 \\ \lambda & \lambda+2\mu & \lambda & 0 & 0 & 0 \\ \lambda & \lambda & \lambda+2\mu & 0 & 0 & 0 \\ 0 & 0 & 0 & \mu - G_C & G_S & 0 \\ 0 & 0 & 0 & G_S & \mu + G_C & 0 \\ 0 & 0 & 0 & 0 & 0 & \mu \end{pmatrix}. \tag{5}$$

Next, we can rotate this tensor to the reference frame of the propagating wave front ($R$, $T$, $k$) (Fig. 3b) and to ($r$, $\Theta$, $\Phi$)-space in which CSEM is defined (Fig. 3c). The perturbed stiffness tensor is set in specific locations in the CSEM mesh. In this process, we ignore small variations in the propagation direction and consider an estimated mean propagation direction. We have tested models in which maximum splitting occurs in the propagation direction and in the horizontal plane of the diffracted part of the ray path; however our preferred model results in maximum splitting for the slightly upward portion of the path in the last part of D″ sampled by $S_{diff}$ on the station side.

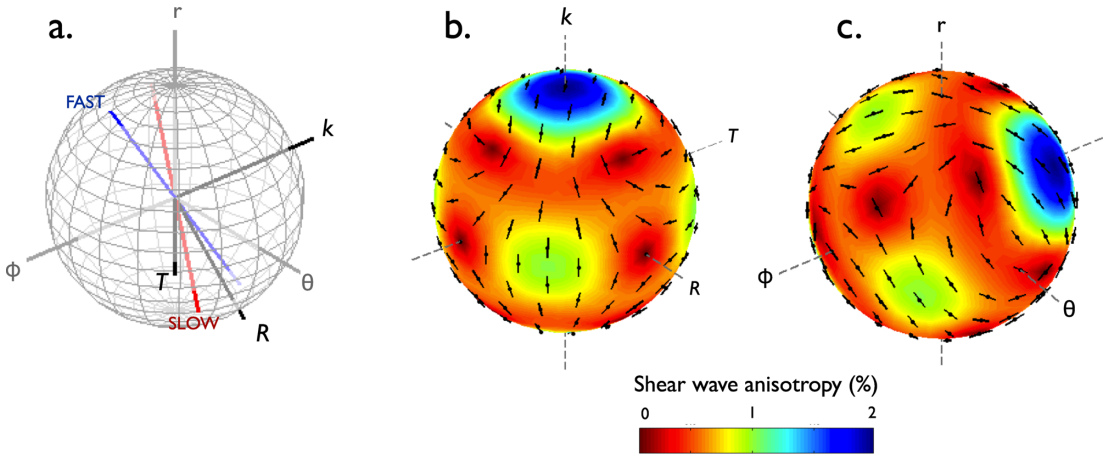


**Figure 3.** (Panel a) Coordinate system for ($R$, $T$, $k$), in which the fast and slow axis are defined, and ($r$, Θ, Φ) in which CSEM is defined. (Panels b and c) Percentage of splitting (in colour) and fast axis direction (black bars) are shown as a function of propagation direction. These are the anisotropic perturbations represented in Model D; 2 per cent splitting and −45° fast axis. Panel (b) is in the ($R$, $T$, $k$) coordinate system, while panel (c) is rotated to the ($r$, Θ, Φ) coordinate system [figure made with MSAT (Walker & Wookey 2012)].

## 3 DATA

### 3.1 1997 September 4 Fiji event

The data for this study come from a deep (∼621 km, $M$w 6.3, 1997 September 4) event near the Fiji islands. The $S_{diff}$ phases from this event are observed at the stations of the Kaapvaal array in southern Africa (see map in Fig. 4). The distance between the event and stations is ∼120°, which is well within the shadow of the core. The radiation pattern and azimuthal range covered are shown in Fig. 5; the azimuth range is non-nodal and the *SH* and *SV* components are expected to be of opposite polarity in all of our data.

This deep event was previously studied for its sensitivity of the $SH_{diff}$ to the LLSVP boundary (Wen 2001; To *et al.* 2005). To *et al.* (2005) pointed out the anomalous elliptical particle motions in $S_{diff}$ outside the LLSVP and linear ones inside the LLSVP. This observation is the focus of this study. Unfortunately, while the Kaapvaal array was deployed, no other suitable nearby events occurred to confirm the observations made here.

### 3.2 Waveforms

$S_{diff}$ waveforms for the transverse (*SH*) and radial (*SV*) components are shown in the first two panels of Fig. 6. These velocity waveforms are filtered between 15 and 100 s. The isotropic velocity jump at the LLSVP boundary is visible in the strong delay occurring in the *SH* phase around an azimuth of 213° (Wen 2001; To *et al.* 2005). To *et al.* (2005) modelled the sharp delay in the waveform and post-cursors with a 4.5 per cent velocity jump across the boundary. At the same time, the waveforms show no evidence of short-period waveform complexities caused by smaller scale ultra-low-velocity zones at this boundary, as has been observed in $S_{diff}$ at the northern boundary of the Pacific LLSVP (Cottaar & Romanowicz 2012).

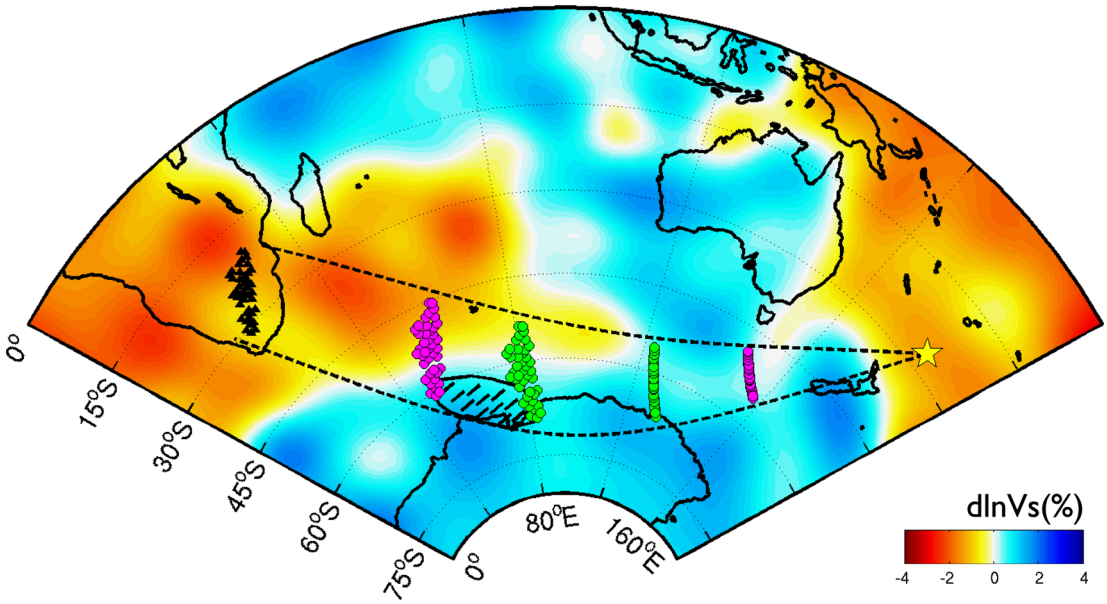


**Figure 4.** Ray path coverage for diffracted waves for the 1997 September 4 Fiji islands events ($M$w 6.3, 621 km depth) observed at the Kaapvaal array in southern Africa. Piercing points for $S_{diff}$ are plotted 150 km above (magenta) and at the core–mantle boundary (green). Background model is SAW24B16 (Mégnin & Romanowicz 2000) at 2750 km depth. Marked patch in the fast region shows the lateral extent of anisotropy in model D5.

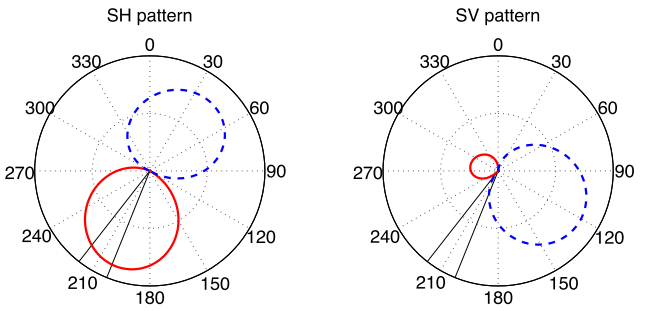


**Figure 5.** Source radiation pattern of $S_{diff}$ waves for 1997 September 4 Fiji Islands event. Source polarity is indicated in blue dashed (positive) and red solid (negative). Azimuths covered in this study are shown by the black solid lines.

The *SV* component of $S_{diff}$ is a much smaller amplitude phase, but appears stronger at azimuths smaller than 206° and greater than 216°. The radiation patterns of *SH* and *SV* have opposite polarities in the direction of interest; the *SH* and *SV* arrivals at stations located at small azimuths have the same polarity, suggesting that the *SV* energy is not the direct *SV* arrival from the source. Small changes in the source could change this interpretation, as the direction of interest lies close to the nodal plane.

Particle motions are shown as a function of azimuth and distance in Fig. 7(a). The data show elliptical anticlockwise particle motions at smaller azimuths and more linear particle motions towards the boundary and inside the LLSVP. Note that the data coverage includes a trend of increasing distance with increasing azimuth.

Figs 7(b) and (c) show the particle motions of core phases *SKS* and *SKKS* for the same event. These phases have similar paths as $S_{diff}$ in the upper mantle, but short, near-vertical paths in D″ within the African LLSVP. The amount of ellipticity in these phases appears scattered, and is different from the trend with azimuth observed for the $S_{diff}$. Silver *et al.* (2001) and Adam & Lebedev (2012) report *SKS* splitting and surface wave azimuthal anisotropy, respectively, across the Kaapvaal array. The measured fast axis trends NNE–SSW in the south, towards ENE–WSW in the centre and then back to NNE–SSW in the north and the splitting time delay is roughly constant, with little variation in the amount of splitting. This trend is different from what we see in the diffracted data. We therefore conclude that the cause of the elliptical particle motions in $S_{diff}$ lies primarily in the lowermost mantle.

### 3.3 Amplitudes

The peak-to-peak amplitudes of $S_{diff}$ on the transverse and radial component and *SKKS* on the radial component are measured in the observed waveforms and synthetics for Preliminary Reference Earth Model (PREM; Dziewonski & Anderson 1981). Results are shown in Fig. 6(c). $SH_{diff}$ (green circles) is the strongest phase. According to the radiation pattern and PREM synthetics, its amplitude should gradually decrease towards larger azimuths. In the observed data, however, strong amplitudes are seen at larger azimuths (and larger distances) due to the lower velocities in the LLSVP.

$SV_{diff}$ (black diamonds) is the weakest phase overall, both in the observed and synthetic waveforms; the observed amplitudes appear to increase towards the smallest azimuths and again slightly at the largest azimuths. The increased amplitude at both ends of the azimuth range differs from the amplitude predictions for PREM. For comparison, *SKKS* amplitudes (brown squares) are plotted. *SKKS* originates as *SV* energy at the source, and its take-off angle is close to that of $SV_{diff}$ (closer than *SKS*). The *SKKS* phase, however, does not show the same trend as $SV_{diff}$ compared to the PREM predictions, as

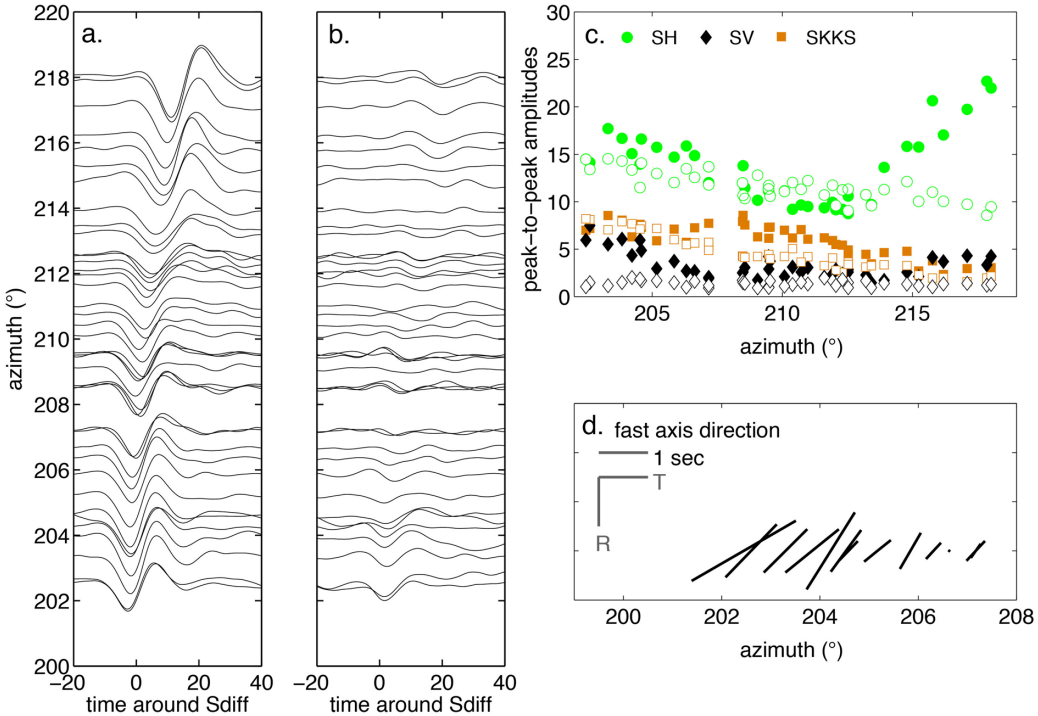


**Figure 6.** Data analysis for the 1997 September 4 Fiji Islands event. (Panel a) Transverse component velocity waveforms around the $S_{diff}$ arrival. Waveforms are filtered between 15 and 100 s. (Panel b) Same as panel (a), but for the radial component. (Panel c) Peak-to-peak amplitude measurements of observed phases (filled symbols) and PREM synthetics (open symbols) for $SH_{diff}$ (green circles), $SV_{diff}$ (black diamonds) and *SKKS* (brown squares). (Panel d) Fast axis direction for $S_{diff}$ phases at smaller azimuths. The length of the lines is scaled to the amount of splitting. Splitting magnitude decreases strongly with azimuth.

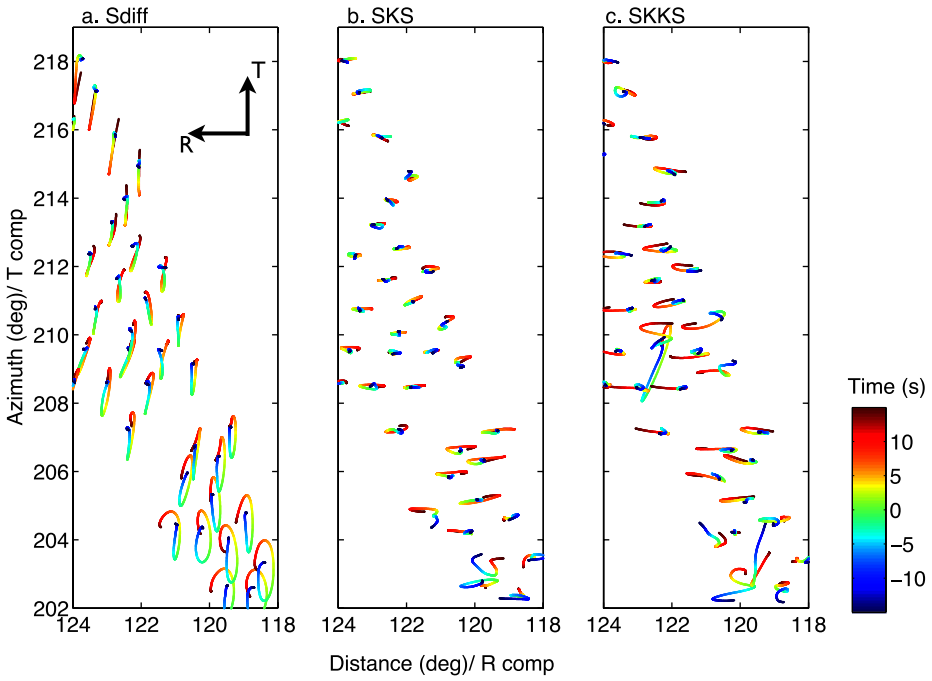


**Figure 7.** Particle motion for $S_{diff}$ (a), *SKS* (b) and *SKKS* (c). Data are filtered between 15 and 100 s and windowed 30 s around the predicted arrival time for the phase. The particle motions are organized by distance and azimuth and the *SH* component deviations are plotted along the vertical axis and the *SV* component along the horizontal axis. Time runs from blue to red on a rainbow scale (see online colour version). The reference times are the 1-D traveltime predictions for PREM.There is no correlation between the ellipticity seen in $S_{diff}$ and in the other two phases.

was already observed in the particle motions, which is an additional argument in favour of a D″ source for the observed $S_{diff}$ anomalies.

The strong energy on the *SV* component, at large azimuths, is associated with linear particle motions (Fig. 7a) in contrast to the elliptical particle motions at small azimuths. We will argue that this energy is not an $SV_{diff}$ phase, but an $SH_{diff}$ arriving out of plane, due to refraction at the LLSVP boundary.

### 3.4 Shear wave splitting results

We quantify the type of anisotropy by measuring the fast axis $\phi$ and splitting time d$t$ with the rotation-correlation method, while comparing to other methods (see Section 2.1). We define the fast axis in the *R-T* plane, as opposed to *N-E*; the latter would interpret the observed splitting to result from apparent anisotropy in the horizontal plane (azimuthal anisotropy). The fast axis $\phi$ is defined as 0° in the transverse direction and positive in the clockwise direction towards the radial direction (looking towards the station, Fig. 2). The orientation of the anisotropy detected here will depend on where along the path the anisotropy occurs. The shear waveforms are sensitive to any anisotropy in the plane orthogonal to the direction of propagation. For the shear wave splitting measurements, the data are filtered between 10 and 30 s.

Remarkably, as reported in To *et al.* (2005), significant splitting only occurs at stations for azimuths less than 208°. These are also the only stations with high-quality splitting index (Wuestefeld *et al.* 2010). The fast axis directions observed for the rotation-correlation method are plotted in Fig. 6(d). The average fast axis direction of these splitting results, weighted by their splitting times, is −46° from the *T* component. Although the quadrant of the fast axis is well constrained, we will later see from the synthetics that there is a great uncertainty in determining the exact fast axis direction. The length of the bars is scaled to the amount of splitting that occurs. There is a strong decrease in the amount of splitting as well as a slight rotation in the fast axis direction with increasing azimuth.

For the stations with strong splitting in $S_{diff}$, there is little (<0.8 s) to no splitting in *SKS* and *SKKS* phases. The $S_{diff}$ and *SK*(*K*)*S* paths are similar in the upper mantle with only a slight difference in incidence angle and their polarizations are orthogonal. If there was a dominant effect of the upper mantle, we would expect these two waves to be split similarly, which is not the case. To perform minor corrections for effects of the upper mantle, a number of assumptions on a simplified anisotropy model would have to be made, with the risk of introducing artificial splitting.

## 4 RESULTS

### 4.1 Excluding isotropic and transverse isotropic models

Initially, we implemented only isotropic velocity variations. Fig. 8 shows a comparison of the observed particle motions versus synthetics for PREM, and synthetics for a saturated version of SAW24B16 (To *et al.* 2005). In the saturated model the positive and negative perturbations away from PREM are saturated to an extreme value. Neither isotropic model reproduces the elliptical particle motions at the smaller azimuths. In contrast to those for the 1-D model PREM, the particle motions for the saturated model capture the traveltime variations due to the LLSVP (seen by the change in colour of the particle motions from more blue to red with azimuth). It also shows some interesting behaviour for the phases that sense the LLSVP boundary around azimuths of 212°–216°. It reproduces the decrease in amplitude and the production of strong post-cursors (To *et al.* 2005). At azimuths around 215°, the

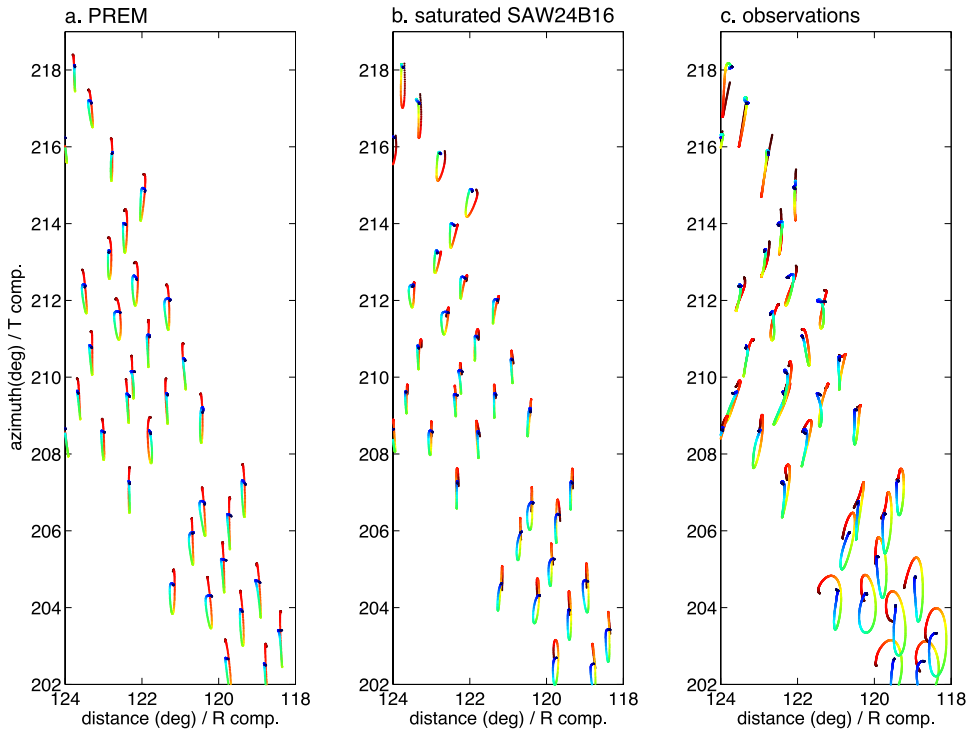


**Figure 8.** Particle motion plots for $S_{diff}$. Both synthetic (a,b) and observed data (c) represented here are filtered between 15 and 100 s. Panel (a) shows the particle motions for PREM and panel (b) for SAW24B16, where the slow LLSVP is saturated at −2.75 per cent and the fast region at +1.00 per cent (comparable to the model found by To *et al.* 2005). Panel (c) shows the observed data. The time range runs from 15 s before to 15 s after the predicted time arrival (from blue to red in the coloured version, colour bar is shown in Fig. 7). The reference times are the 1-D traveltime predictions for PREM. Both isotropic models result in nearly linear particle motions.

coarrival of the main phases and post-cursors results in an apparent elliptical particle motion. This interference is not present in the real data where the post-cursor appears as a separate phase with a larger traveltime delay at slightly smaller azimuths (see Fig. 6). These post-cursors fall outside the time window for the determination of the particle motions. We will, however, find them in the synthetic waveforms for our best model in Fig. 11. The difference in behaviour of the post-cursors between the observations and synthetics could be due to the lateral sharpness of the isotropic velocity jump, or to the exact shape of the LLSVP boundary. We refrain from modelling the post-cursors more precisely here (see also To *et al.* 2005).

All the stations are located at distances larger than 118°. These are far within the core shadow of direct shear wave arrivals, and $SV_{diff}$ energy is not expected to propagate that far along the CMB (see Fig. 1). As expected, synthetic particle motions in Fig. 8 show no $SV_{diff}$ arrival for PREM (panel a) or for a saturated isotropic model (panel b).

To propagate *SV* diffracted energy over larger distances along the CMB, the velocity model needs to be slower than PREM. The strong $SV_{diff}$ arrivals observed are, however, for paths outside the African LLSVP, where the shear velocity is faster than average in D″. We attempted to model the strong $SV_{diff}$ arrivals at large distances by introducing radial anisotropy with *SV* velocity slower than *SH* velocity. The blue synthetics in Fig. 1 are for such a model. They show that the integrated traveltime difference between the *SH* and *SV* become significant; at larger distances the two phases become more than a wavelength apart. As there is no overlap between the two phases, the anisotropy is too strong to result in an elliptical particle motion.

More complex anisotropy in the lowermost mantle can cause splitting of $SH_{diff}$ and elliptical particle motions at large distances in the core shadow. In the following sections, we present attempts to model the nature of this anisotropy, insofar as our data can constrain this.

### 4.2 Anisotropic models

We first note that we constrain the anisotropy to be located primarily in the part of D″ where the phase turns up towards the station. We attempted to introduce anisotropy in the diffracted part of the path, but the coupling between the *SH* and *SV* component, and the subsequent loss of amplitude due to this coupling and the coupling of the *SV* component with the outer core, leads to overall smaller amplitudes in the synthetics. We do not observe decreased amplitudes in the observations. The opposite is true: for the smaller azimuths, both the *SH* and *SV* components have stronger amplitudes than predicted for PREM (see Fig. 6b).

We present several models with anisotropy added to the saturated isotropic model. The anisotropy is confined to the faster-than-average region outside the African LLSVP. The resulting particle motions are plotted in Fig. 9. The model parameters are summarized in Table 1.

Model A performs well, with the fast and slow axis defined in the horizontal plane. The anisotropy in the stiffness tensor is defined similarly to the other models, but the maximum splitting is rotated to be along the radial component and not in the direction of propagation of the $S_{diff}$ phase. The fast axis is N–S and the slow axis E–W; the two differ in shear velocity by 10 per cent. The third axis has an intermediate velocity. This model of anisotropy produces

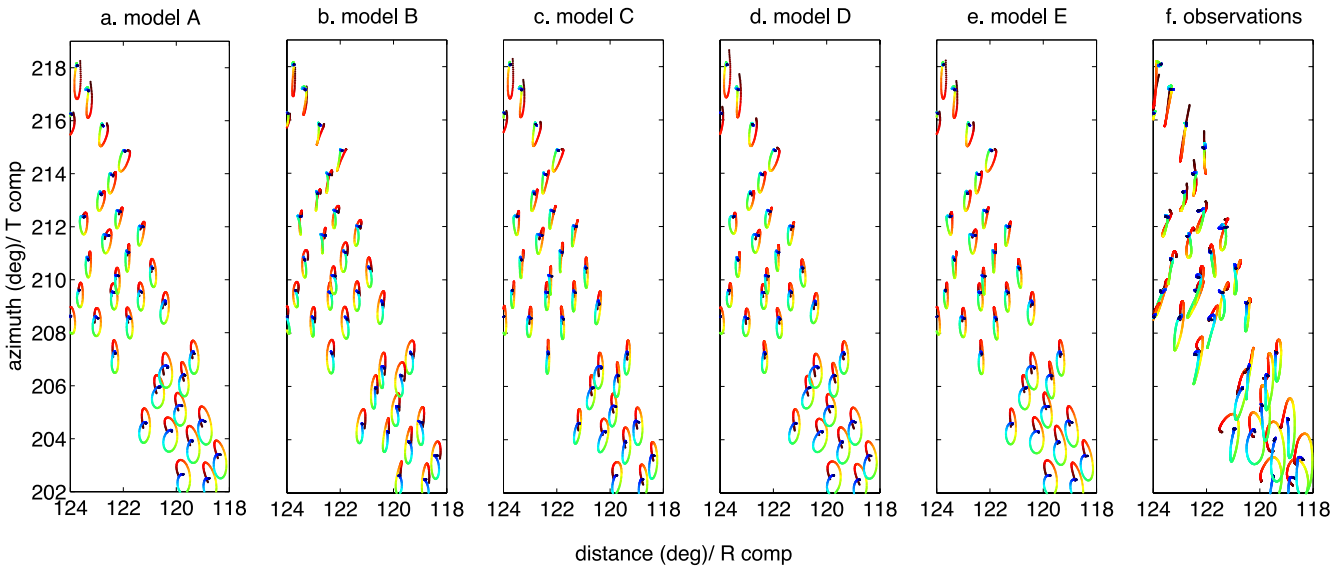


**Figure 9.** Particle motion plots for $S_{\rm diff}$ for synthetic models including anisotropy. Model A includes purely azimuthal anisotropy with a fast N–S axis. Models B–E include anisotropy orthogonal to the direction of propagation, with fast axis directions of $+45^\circ$, $-65^\circ$, $-45^\circ$ and $-25^\circ$, respectively. Observed particle motions are shown in panel (f). Time increases from blue to red (see colour bar in Fig. 7). The reference times are the 1-D traveltime predictions for PREM.

**Table 1.** Selected anisotropy models. Fast axis, strength of anisotropy and their radial and lateral extent are listed. Model A is an exception as its fast and slow axis are defined in the horizontal plane as opposed to the plane orthogonal to the direction of propagation in the data. The shear wave splitting results are for stations at azimuths smaller than $208^\circ$. $\phi_{\rm f}$ is an average measured fast axis weighted by their splitting times d$t$ (giving emphasis to the more robust stations with higher splitting times).

| Model | Fast axis $\phi_{\rm f}$ | Per cent of anisotropy | Radial extent (km) | Lateral constraint (per cent) | Measured $\phi_{\rm f}$ | Measured d$t$ (s) |
|---|---|---|---|---|---|---|
| A | $0^\circ$ (azimuth) | 10 | 370 | $\mathrm{d}\ln V > 0$ | $-35^\circ$ | 2.3 |
| B | $45^\circ$ | 4 | 370 | $\mathrm{d}\ln V > 0$ | $48^\circ$ | 1.3 |
| C | $-65^\circ$ | 4 | 370 | $\mathrm{d}\ln V > 0$ | $-43^\circ$ | 1.28 |
| D | $-45^\circ$ | 4 | 370 | $\mathrm{d}\ln V > 0$ | $-37^\circ$ | 2.3 |
| E | $-25^\circ$ | 4 | 370 | $\mathrm{d}\ln V > 0$ | $-44^\circ$ | 1.6 |
| D1 | $-45^\circ$ | 8 | 100 | $\mathrm{d}\ln V > 0$ | $-46^\circ$ | 1.4 |
| D2 | $-45^\circ$ | 8 | 150 | $\mathrm{d}\ln V > 0$ | $-36^\circ$ | 1.7 |
| D3 | $-45^\circ$ | 8 | 200 | $\mathrm{d}\ln V > 0$ | $-29^\circ$ | 2.6 |
| D4 | $-45^\circ$ | 8 | 150 | $\mathrm{d}\ln V > 1.0$ | $-45^\circ$ | 0.65 |
| D5 | $-45^\circ$ | 8 | 150 | $\mathrm{d}\ln V > 0.5$ | $-44^\circ$ | 1.0 |

particle motions that are comparable to those observed. If the fast axis is rotated by $\sim 45^\circ$ in either direction in the horizontal plane, the polarity of the particle motion switches sign. This model illustrates the non-uniqueness of the elastic tensor. In this case, where the strongest anisotropy is defined in the horizontal plane, correct splitting along the direction of propagation is obtained for our data set. We call this the apparent splitting of the anisotropy model. The maximum splitting will always occur for shear waves propagating orthogonal to the plane in which we define the azimuthal anisotropy (as long as its polarization is not parallel to the fast or slow axis). The apparent anisotropic splitting for shear waves in other planes will always be smaller.

We continue with models that have anisotropy variations defined in the plane orthogonal to the direction of propagation (panels a and b in Fig. 3). In this case, the maximum anisotropy in the tensor and the apparent anisotropy along the direction of propagation will be the same, thus the model captures the part of the anisotropic tensor that is constrained by our data set; it is unlikely to be the true, complete anisotropic tensor.

We estimate a suitable propagation direction from the azimuth and incidence angle of the diffracted waveforms at 100 km above the CMB, as they turn up towards the stations. This results in an azimuth of $310^\circ$ and an upward angle of $30^\circ$. Models B–E all have a fast and slow axis defined in the plane orthogonal to this direction. The four models have fast axis directions of $+45^\circ$, $-65^\circ$, $-45^\circ$ and $-25^\circ$, respectively. All models have 4 per cent velocity difference between the fast and the slow axis. Our shear wave splitting measurements suggest a mean fast axis direction of $-46^\circ$ in the plane considered.

Model B has a fast axis of $+45^\circ$. This model, as can be expected, produces particle motions that are opposite from those observed. Model D, with a fast axis at $-45^\circ$ is, as expected, the best model in terms of the orientation of the particle motions and in the shear wave splitting measurements. Models C and E are presented to illustrate the change in waveforms with a shift of $20^\circ$ in fast axis direction. The particle motions only differ slightly from model D. From the shear wave splitting measurements, listed in Table 1, we find that it is hard to distinguish between models with slight differences in fast axis. This shows the limitations of the method and data. When comparing the particle motions, Model D performs best.

### 4.3 Lateral and radial constraints

So far we have constrained the anisotropy to the lowermost 370 km and to the fast region outside the LLSVP. Here we investigate further

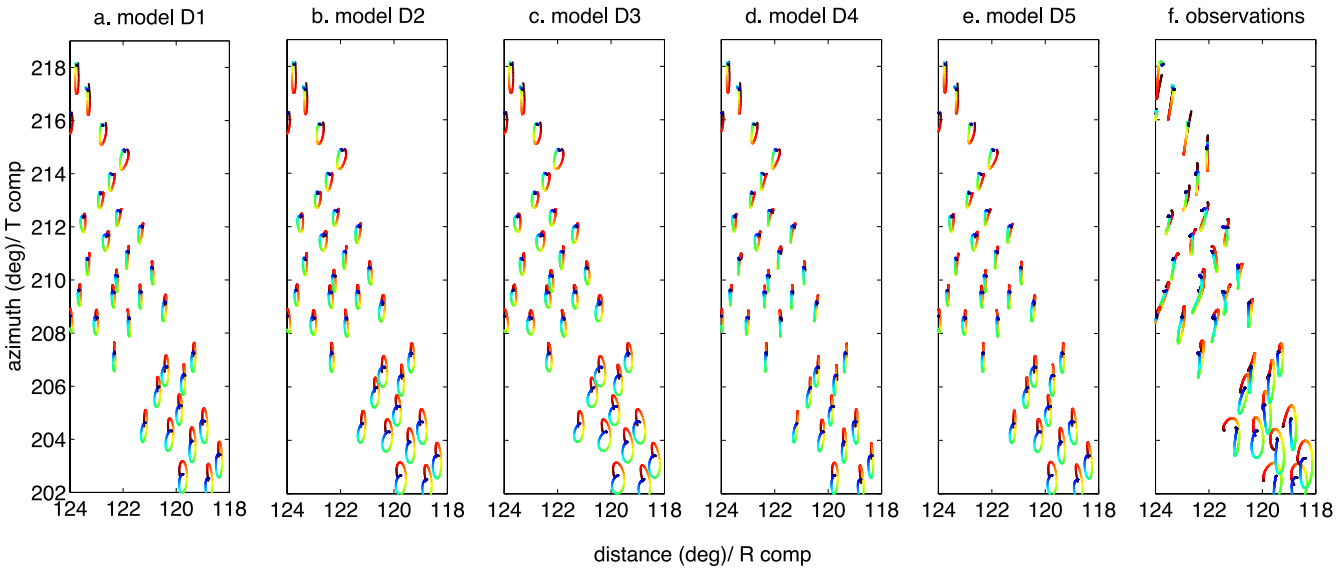


**Figure 10.** Particle motion plots for $S_{\rm diff}$ in models with anisotropy confined in the lateral and radial direction. All models have a fast axis direction of −45°. Model D1-3 include 8 per cent of anisotropy over 100, 150 and 200 km, respectively, above the core–mantle boundary. Models D4–5 have fixed anisotropy of 8 per cent over 150 km, but confine the anisotropy laterally to the region where d ln $V$ is greater than 1.0 per cent (D4) and greater than 0.5 per cent (D5). Observed particle motions are shown in panel (f). Time increases from blue to red (see colour bar in Fig. 7). The reference times are the 1-D traveltime predictions for PREM.

constraints on the lateral and radial extent of the anisotropy. We keep the fast axis fixed at −45°.

So far the models had 4 per cent velocity difference between the fast and slow axis over the entire 370-km thickness of the layer. In Models D1–D3 (Fig. 10), we vary the extent of the anisotropic layer in the radial direction above the CMB. These models extend over 100 (D1), 150 (D2) and 200 km (D3) with 8 per cent anisotropic strength. From the ellipticity of the particle motions and the mean measured splitting times (in Table 1), one can see an increase of splitting time with thickness of the anisotropic layer. These examples illustrate the trade-off between thickness and the strength of anisotropy, and the difficulty to constrain both.

In models D1–D3, the splitting extends to larger azimuths than in the data. This suggests that the anisotropy does not extend with the same strength as far towards the LLSVP boundary as implemented in the model. Models D4 and D5 constrain the anisotropy laterally to the region in which the isotropic shear wave deviation from PREM is >1.0 per cent and 0.5 per cent, respectively. Model D5 does the best job in capturing the azimuthal extent of the splitting in the observations.

### 4.4 Preferred model

Our preferred model, D5, captures many of the features seen in the data. Fig. 11 shows the waveforms, amplitudes and measured fast axis directions and magnitudes. These can be directly compared to the same analysis on the observed data shown in Fig. 6.

The fast axis direction, as well as the decrease in splitting time with azimuth, are well reproduced by this model. This can also be seen in the strength and polarity of the *SV* component at smaller azimuths. Post-cursors are also generated on the *SH* component at intermediate azimuths. This feature is stronger in synthetics than in the observations.

There are two aspects of the observations that our model does not capture. One is that the *SH* component at smaller azimuths is stronger in the observations than predicted by this synthetic model or by PREM (Fig. 8a). This could be a source effect. A stronger *SH* component would also lead to a stronger *SV* component after splitting. The other is that the polarity of the energy on the *SV* component at large azimuths is opposite to that in the observations. This means the rotation of the backazimuth of the $SH_{\rm diff}$ arrival is opposite in the synthetics as compared to the observations. As these rotations are caused by refraction at the LLSVP boundary, fixing the polarity would require more detailed modelling of the specific shape of the LLSVP boundary, which is beyond the scope of this study.

Our preferred model has additional elliptical particle motions around azimuths of 212°–216°. As discussed in Section 4.1 and shown in Fig. 8(b), these elliptical particle motions result from the saturation of the LLSVP boundary and the interference of the main phase and a post-cursor.

## 5 DISCUSSION AND CONCLUSIONS

One possible cause of azimuthal anisotropy in the lowermost mantle is shape-preferred orientation (SPO) due to layering or aligned inclusions (Kendall & Silver 1998). Hall *et al.* (2004) measure anisotropic strength in various scenarios, to explain observed *SK(K)S* splitting. They find that low-velocity inclusions such as melt, are more effective at producing azimuthal anisotropy than solid, fast inclusions. Melt inclusions, however, are more likely within the LLSVP than in the fast region, where we observe anisotropy, as such inclusions should lower the overall average shear wave velocity.

A second option is the alignment of intrinsically anisotropic minerals, that is, lattice-preferred orientation (LPO), the common explanation for azimuthal anisotropy in the upper mantle. LPO becomes more likely in regions where strong deformation is currently occurring. Dislocation creep is more likely to occur in cold slabs

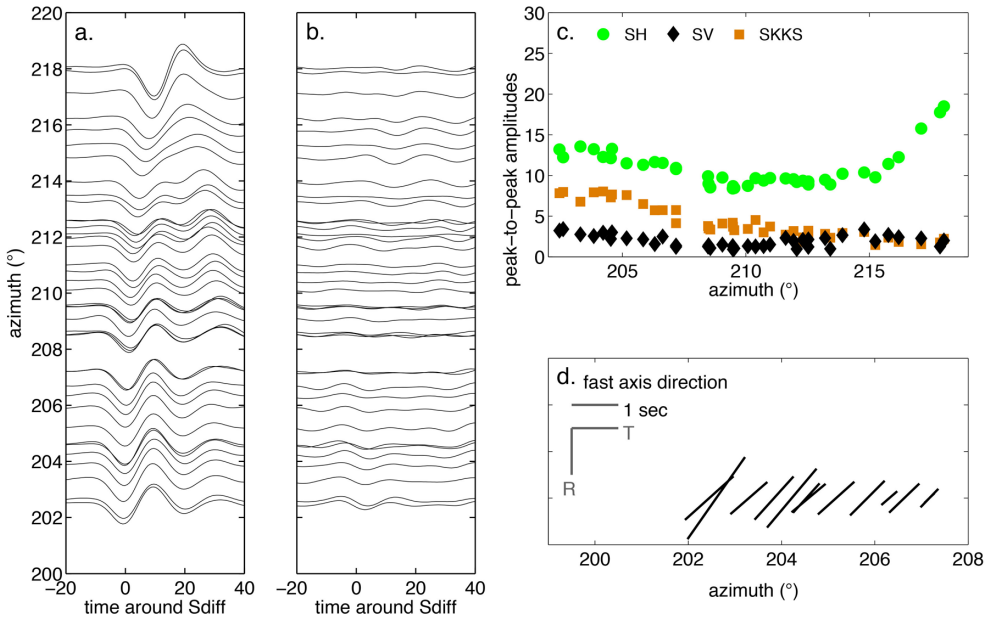


**Figure 11.** Synthetic data analysis for our preferred model—D5. (Panel a) Transverse component velocity waveforms around the $S_{diff}$ arrival. Synthetic waveforms are filtered between 15 and 100 s. (Panel b) Same as panel (a), but for the radial component. (Panel c) Peak-to-peak amplitude measurements of synthetic phases for $SH_{diff}$ (green circles), $SV_{diff}$ (black diamonds) and *SKKS* (brown squares). (Panel d) Fast axis direction in the synthetic data at smaller azimuths. The length of the lines is scaled to the amount of splitting.

(McNamara *et al.* 2001) and large strains can occur in slabs rotating onto the CMB (Walker *et al.* 2011; Wenk *et al.* 2011). Azimuthal anisotropy has generally been observed within the ring of fast velocities at the base of the mantle; that is, locations that are more likely to include slab remnants (e.g. Rokosky *et al.* 2006; Long 2009; Nowacki *et al.* 2011). Geodynamical modelling constrained by past plate tectonics shows that there could be slab remnants in the region studied beneath the Indian/Antarctic Ocean, resulting from subduction that ceased 80 Ma (Steinberger & Torsvik 2012).

What mineral assemblages within the slab would cause the significant anisotropy documented here? The single crystal shear wave azimuthal anisotropy is roughly twice as strong in pPv as in Pv (Iitaka *et al.* 2004; Tsuchiya *et al.* 2004). The occurrence of pPv in D″ would also be more likely in faster than average, colder regions. Both Pv and pPv would also cause strong, and opposite signatures in radial anisotropy (Wenk *et al.* 2011).

Global models of radial anisotropy (Panning & Romanowicz 2006; Kustowski *et al.* 2008) do not indicate a strong signature in our area of study, although the data coverage in this region is far from ideal. The decrease in strength of anisotropy towards the LLSVP boundary could mean that the slab material—and with that the fast direction—is rotating to a plane to which our data have no sensitivity (Fig. 12). Rotation by material flow could happen if the boundary is a mechanical boundary, possibly due to compositionally distinct LLSVPs. Wang & Wen (2007) find patterns of complex azimuthal anisotropy near the African LLSVP from differential *SK*(*K*)*S* splitting, showing further evidence for complex flow patterns outside this structure.

In our data set, there is no apparent anisotropy within the LLSVP. Either our data set has no sensitivity to the anisotropy present, or the convection in the LLSVP is too weak, too small-scale, or the material's intrinsic anisotropy is too weak.

We have constrained a patch of strong tilted anisotropy south of the African LLSVP from observations of shear-diffracted phases at large distances. The fast axis of the anisotropy is tilted to the north away from the direction of propagation to the northwest. The azimuthal anisotropy decreases in strength or rotates towards the boundary of the LLSVP. No anisotropy is observed within the LLSVP. The occurrence of pPv in slab remnants is consistent with the fast velocities and strong azimuthal anisotropy, while a compositionally distinct LLSVP is likely to affect flow patterns near its border.

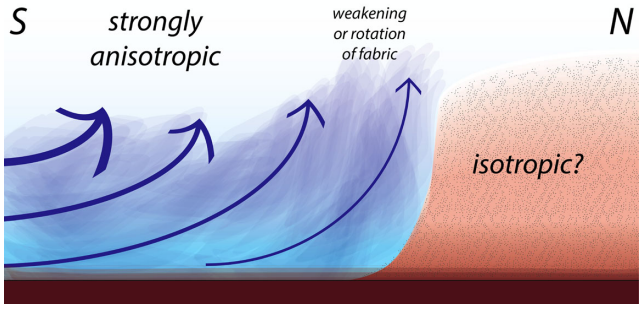


**Figure 12.** Cartoon cross-section from south to north through the edge of the African LLSVP. Possible flow outside the LLSVP as suggested by the observed anisotropy.

## ACKNOWLEDGEMENTS

The data for this project came from Incorporated Research Institutions for Seismology (www.iris.edu). We thank Yann Capdeville for providing the CSEM code which produced the synthetic data in this study. Shear wave measurements are done with help of the SplitLab Matlab package (www.gm.univ-montp2.fr/splitting/). Fig. 3 is produced with the MSAT Matlab package (www1.gly.bris.ac.uk/MSAT/). This work was supported by NSF/CSEDI grant 1067513 and ERC grant 'WAVETOMO'. Berkeley Seismological Laboratory contribution number 13-9.

## REFERENCES


Adam, J. & Lebedev, S., 2012. Azimuthal anisotropy beneath southern Africa from very broad-band surface-wave dispersion measurements, *Geophys. J. Int.,* **191**(1), 155–174.

Bowman, J.R. & Ando, M., 1987. Shear-wave splitting in the upper-mantle wedge above the Tonga subduction zone, *Geophys. J. Int.,* **88**(1), 25–41.

Capdeville, Y., Larmat, C., Vilotte, J.P. & Montagner, J.P., 2002. A new coupled spectral element and modal solution method for global seismology—a first application to the scattering induced by a plume-like anomaly, *Geophys. Res. Lett.,* **29,** 1318–1322.

Capdeville, Y., To, A. & Romanowicz, B., 2003. Coupling spectral elements and modes in a spherical Earth: an extension to the 'sandwich' case, *Geophys. J. Int.,* **154**(1), 44–57.

Cottaar, S. & Romanowicz, B., 2012. An unusually large ULVZ at the base of the mantle near Hawaii, *Earth planet. Sci. Lett.,* **355,** 213–222.

Crampin, S., 1984. Effective anisotropic elastic constants for wave propagation through cracked solids, *Geophys. J. Int.,* **76**(1), 135–145.

Doornbos, D. & Mondt, J., 1980. The interaction of elastic waves with a solid-liquid interface, with applications to the core-mantle boundary, *Pure appl. Geophys.,* **118**(2), 1293–1309.

Dziewonski, A.M. & Anderson, D.L., 1981. Preliminary reference Earth model, *Phys. Earth planet. Inter.,* **25**(4), 297–356.

Garnero, E. & Lay, T., 1997. Lateral variations in lowermost mantle shear wave anisotropy, *J. geophys. Res,* **102,** 8121–8135.

Garnero, E., Maupin, V., Lay, T. & Fouch, M., 2004. Variable azimuthal anisotropy in Earth's lowermost mantle, *Science,* **306**(5694), 259–261.

Garnero, E.J. & McNamara, A.K., 2008. Structure and dynamics of Earth's lower mantle, *Science,* **320**(5876), 626–628.

Hall, S., Kendall, J. & van der Baan, M., 2004. Some comments on the effects of lower-mantle anisotropy on SKS and SKKS phases, *Phys. Earth planet. Inter.,* **146**(3–4), 469–481.

Iitaka, T., Hirose, K., Kawamura, K. & Murakami, M., 2004. The elasticity of the $MgSiO_3$ post-perovskite phase in the Earth's lowermost mantle, *Nature,* **430**(6998), 442–445.

Karato, S., 1998a. Some remarks on the origin of seismic anisotropy in the D″ layer, *Earth Planets Space,* **50,** 1019–1028.

Karato, S., 1998b. Seismic anisotropy in the deep mantle, boundary layers and the geometry of mantle convection, *Pure appl. Geophys.,* **151**(2–4), 565–587.

Karato, S., Jung, H., Katayama, I. & Skemer, P., 2008. Geodynamic significance of seismic anisotropy of the upper mantle: new insights from laboratory studies, *Annu. Rev. Earth planet. Sci.,* **36,** 59–95.

Kawai, K. & Geller, R.R.J., 2010. The vertical flow in the lowermost mantle beneath the Pacific from inversion of seismic waveforms for anisotropic structure, *Earth planet. Sci. Lett.,* **297**(1–2), 190–198.

Kendall, J. & Silver, P., 1998. Investigating causes of D″ anistropy, *Geodyn. Ser.,* **28,** 97–118.

Komatitsch, D., Vinnik, L.P. & Chevrot, S., 2010. SHdiff-SVdiff splitting in an isotropic Earth, *J. geophys. Res.,* **115,** B07312, doi:10.1029/2009JB006795.

Kustowski, B., Ekström, G. & Dziewonski, A., 2008. Anisotropic shear-wave velocity structure of the Earth's mantle: a global model, *J. geophys. Res.,* **113**(B6), B06306, doi:10.1029/2007JB005169.

Lekic, V., Cottaar, S., Dziewonski, A.M. & Romanowicz, B., 2012. Cluster analysis of global lower mantle tomography: a new class of structure and implications for chemical heterogeneity, *Earth planet. Sci. Lett.,* **357–358,** 68–77.

Long, M.D., 2009. Complex anisotropy in D″ beneath the eastern Pacific from SKS-SKKS splitting discrepancies, *Earth planet. Sci. Lett.,* **283**(1–4), 181–189.

Loubet, N., Ribe, N. & Gamblin, Y., 2009. Deformation modes of subducted lithosphere at the core-mantle boundary: an experimental investigation, *Geochem. Geophys. Geosyst.,* **10**(10), Q10004, doi:10.1029/2009GC002492.

Lynner, C. & Long, M., 2012. Evaluating contributions to SK(K)S splitting from lower mantle anisotropy: a case study from Station DBIC, Côte D'Ivoire, *Bull. seism. Soc. Am.,* **102,** 1030–1040.

Mainprice, D., 2007. Seismic anisotropy of the deep Earth from a mineral and rock physics perspective, in *Treatise on Geophysics,* Vol. **2,** pp. 437–492, ed. Shubert, G., Elsevier.

Mainprice, D., Barruol, G. & Ismail, W., 2000. The seismic anisotropy of the Earth's mantle: from single crystal to polycrystal, in *Geophysical Monograph Series,* Vol. **117,** pp. 237–264, AGU.

Maupin, V., 1994. On the possibility of anisotropy in the D″ layer as inferred from the polarization of diffracted S waves, *Phys. Earth planet. Inter.,* **87**(1–2), 1–32.

Maupin, V., 2005. Azimuthal anisotropy in the D″ layer beneath the Caribbean, *J. geophys. Res.,* **110**(B8), 1–20.

McNamara, A.A.K., Karato, S.S.-I., van Keken, P. & van Keken, P.E., 2001. Localization of dislocation creep in the lower mantle: implications for the origin of seismic anisotropy, *Earth planet. Sci. Lett.,* **191**(1–2), 85–99.

McNamara, A.K. & Zhong, S., 2005. Thermochemical structures beneath Africa and the Pacific Ocean, *Nature,* **7062,** 1136–1139.

Mégnin, C. & Romanowicz, B., 2000. The three-dimensional shear velocity structure of the mantle from the inversion of body, surface and higher-mode waveforms, *Geophys. J. Int.,* **143**(3), 709–728.

Miyagi, L., Kanitpanyacharoen, W., Stackhouse, S., Militzer, B. & Wenk, H.-R., 2011. The enigma of post-perovskite anisotropy: deformation versus transformation textures, *Phys. Chem.,* **38**(9), 665–678.

Montagner, J., 1998. Where can seismic anisotropy be detected in the Earth's mantle? in boundary layers, *Pure appl. Geophys.,* **151**(2–4), 223–256.

Montagner, J., Griot-Pommera, D. & Lavé, J., 2000. How to relate body wave and surface wave anisotropy? *J. geophys. Res.,* **105**(88), 19 015–19 019.

Morelli, A., Dziewonski, A.M. & Woodhouse, J.H., 1986. Anisotropy of the inner core inferred from PKIKP travel times, *Geophys. Res. Lett.,* **13**(13), 1545–1548.

Mosca, I., Cobden, L., Deuss, A., Ritsema, J. & Trampert, J., 2012. Seismic and mineralogical structures of the lower mantle from probabilistic tomography, *J. geophys. Res.,* **117,** B06304, doi:10.1029/2011JB008851.

Niu, F. & Perez, A., 2004. Seismic anisotropy in the lower mantle: a comparison of waveform splitting of SKS and SKKS, *Geophys. Res. Lett.,* **31,** L24612, doi:10.1029/2004GL021196.

Nowacki, A., Wookey, J. & Kendall, J., 2010. Deformation of the lowermost mantle from seismic anisotropy, *Nature,* **467**(7319), 1091–1094.

Nowacki, A., Wookey, J. & Kendall, J.-M.J., 2011. New advances in using seismic anisotropy, mineral physics and geodynamics to understand deformation in the lowermost mantle, *J. Geodyn.,* **52**(3–4), 205–228.

Panning, M. & Romanowicz, B., 2006. A three-dimensional radially anisotropic model of shear velocity in the whole mantle, *Geophys. J. Int.,* **167**(1), 361–379.

Restivo, A. & Helffrich, G., 2006. Core–mantle boundary structure investigated using SKS and SKKS polarization anomalies, *Geophys. J. Int.,* **165**(1), 288–302.

Rokosky, J.M., Lay, T. & Garnero, E.J., 2006. Small-scale lateral variations in azimuthally anisotropic D″ structure beneath the Cocos Plate, *Earth planet. Sci. Lett.,* **248**(1–2), 411–425.

Silver, P. & Chan, W., 1991. Shear wave splitting and subcontinental mantle deformation, *J. geophys. Res.,* **96**(B10), 16 429–16 454.

Silver, P., Gao, S. & Liu, K., 2001. Mantle deformation beneath southern Africa, *Geophys. Res. Lett.,* **28**(13), 2493–2496.

Stackhouse, S., Brodholt, J.P., Wookey, J., Kendall, J.-M. & Price, G.D., 2005. The effect of temperature on the seismic anisotropy of the perovskite and post-perovskite polymorphs of $MgSiO_3$, *Earth planet. Sci. Lett.,* **230**(1–2), 1–10.

Steinberger, B. & Torsvik, T.H., 2012. A geodynamic model of plumes from the margins of Large Low Shear Velocity Provinces, *Geochem. Geophys. Geosyst.,* **13,** Q01W09, doi:10.1029/2011GC003808.

Teng, T.-L. & Richards, P., 1976. Diffracted P, *SV* and *SH* waves and their shadow boundary shifts, *J. geophys. Res.,* **74**(6), 1537–1555.

Thomas, C., Wookey, J. & Simpson, M., 2007. D″ anisotropy beneath Southeast Asia, *Geophys. Res. Lett,* **34**(4), L04301, doi:10.1029/2006GL028965.

To, A., Romanowicz, B., Capdeville, Y. & Takeuchi, N., 2005. 3D effects of sharp boundaries at the borders of the African and Pacific Superplumes: observation and modeling, *Earth planet. Sci. Lett.,* **233**(1–2), 1447–1460.

Trampert, J. & van Heijst, H., 2002. Global azimuthal anisotropy in the transition zone, *Science,* **296**(5571), 1297–1299.

Tsuchiya, T., Tsuchiya, J., Umernote, K. & Wentzcovitch, R., 2004. Phase transition in $MgSiO_3$ perovskite in the Earth's lower mantle, *Earth planet. Sci. Lett.,* **224**(3), 241–248.

Vinnik, L., Farra, V. & Romanowicz, B., 1989. Observational evidence for diffracted *SV* in the shadow of the Earth's core, *Geophys. Res. Lett.,* **16**(6), 519–522.

Vinnik, L., Romanowicz, B., Le Stunff, Y. & Makeyeva, L., 1995. Seismic anisotropy in the D″ layer, *Geophys. Res. Lett.,* **22**(13), 1657–1660.

Walker, A. & Wookey, J., 2012. MSAT-A new toolkit for the analysis of elastic and seismic anisotropy, *Comput. Geosci.,* **49,** 81–90.

Walker, A.M., Forte, A.M., Wookey, J., Nowacki, A. & Kendall, J.-M., 2011. Elastic anisotropy of D″ predicted from global models of mantle flow, *Geochem. Geophys. Geosyst.,* **12**(10), 1–22.

Wang, Y. & Wen, L., 2007. Complex seismic anisotropy at the border of a very low velocity province at the base of the Earth's mantle, *J. geophys. Res.,* **112**(B9), 1–11.

Wen, L., 2001. Seismic evidence for a rapidly varying compositional anomaly at the base of the Earth's mantle beneath the Indian Ocean, *Earth planet. Sci. Lett.,* **194**(1–2), 83–95.

Wenk, H.-R., Cottaar, S., Tomé, C.N., McNamara, A. & Romanowicz, B., 2011. Deformation in the lowermost mantle: from polycrystal plasticity to seismic anisotropy, *Earth planet. Sci. Lett.,* **306**(1–2), 33–45.

Wentzcovitch, R.M., Tsuchiya, T. & Tsuchiya, J., 2006. $MgSiO_3$ postperovskite at D″ conditions., *Proc. Natl. Acad. Sci.,* **103**(3), 543–546.

Woodhouse, J.H., Giardini, D. & Li, X.D., 1986. Evidence for inner core anisotropy from free oscillations, *Geophys. Res. Lett.,* **13**(13), 1549–1552.

Wookey, J. & Kendall, J., 2008. Constraints on lowermost mantle mineralogy and fabric beneath Siberia from seismic anisotropy, *Phys. Earth planet. Inter.,* **275**(1), 32–42.

Wuestefeld, A., Al-Harrasi, O., Verdon, J.P., Wookey, J. & Kendall, J., 2010. A strategy for automated analysis of passive microseismic data to image seismic anisotropy and fracture characteristics, *Geophys. Prospect.,* **58,** 755–773.

Wüstefeld, A., Bokelmann, G., Zaroli, C. & Barruol, G., 2008. SplitLab: a shear-wave splitting environment in Matlab, *Comput. Geosci.,* **34**(5), 515–528.